Computer-based three-dimensional visualization of developmental gene expression

Johannes Streicher[1], Markus A. Donat[1], Bernhard Strauss[1], Ralf Spörle[2], Klaus Schughart[3] & Gerd B. Müller[1]

A broad understanding of the relationship between gene activation, pattern formation and morphogenesis will require adequate tools for three-dimensional and, perhaps four-dimensional, representation and analysis of molecular developmental processes. We present a novel, computer-based method for the 3D visualization of embryonic gene expression and morphological structures from serial sections. The information from these automatically aligned 3D reconstructions exceeds that from single-section and whole-mount visualizations of *in situ* hybridizations. In addition, these 3D models of gene-expression patterns can become a central component of a future developmental database designed for the collection and presentation of digitized, morphological and gene-expression data. This work is accompanied by a web site (http://www.univie.ac.at/GeneEMAC).

A detailed spatio-temporal analysis of embryonic gene expression will likely reveal the actual role of developmental genes in controlling morphological organization. This calls for reliable tools that can visualize high-resolution gene-expression patterns in a 3D morphogenetic context. At the same time, this graphical information should be permanently stored in a digital format, to be universally accessible via the Internet and directly linked with sequence and text-format gene databases[1,2].

The analysis of organismal structures by sectioning techniques has always suffered from the loss of 3D information of the details visible in single microscopic images and has led to the development of numerous reconstruction methods (refs 3–21 and http://biocomp.stanford.edu/3dreconstruction/refs/drushel93.txt). In these techniques, a fundamental problem is the objective realignment of inherently unaligned and distorted sections. Virtual sectioning techniques, such as computer tomography (CT), magnetic resonance imaging (MRI) and confocal laser scanning microscopy (CLSM), do not have this problem, because they provide inherently registered sectional images. Advances in miniaturizing MRI technology permit non-invasive views of embryonic structures with resolutions approaching low-magnification light microscopy[2,22], but these techniques cannot be used to visualize gene-expression signals. Confocal microscopy, on the other hand, currently does not allow visualization of the morphological context simultaneously with the fluorescent signals, and is limited with regard to specimen size.

The GeneEMAC technique

Here we present a novel method for the concerted, high-resolution, 3D visualization of gene-expression signals and morphological information from embryonic serial sections. The major technical innovation of our method consists of the rapid and objective realignment (automatic congruencing) of sections and the high degree of automation achieved in the feature extraction and reconstruction processes. The method is based on external marker-based automatic congruencing[19] (EMAC) and is therefore termed 'GeneEMAC'. Because whole-mount *in situ* hybridization (WISH) currently is the standard technique for the visualization of gene-expression patterns in the embryo, our method relies on serially sectioned WISH preparations (Fig. 1*a*). GeneEMAC combines the high resolution of histological sections with the methodological advantages of whole-mount staining. Grey-scale images of phase-contrast and bright-field views of serial sections through glycol-methacrylate–embedded WISH embryos provide the starting point for computer reconstruction. After capturing images of histological sections, the computer automatically performs all further image-processing operations, such as section orientation and the extraction of hybridization signals and high-contrast morphological boundaries. This approach largely eliminates interactive processing by an operator and thus improves objectivity and time expense.

The GeneEMAC method covers the full range of structural levels studied in developmental research. We demonstrate here reconstructions of gene-expression patterns in combination with morphological landmarks at three different structural levels. At the level of small developmental subunits, we have reconstructed the expression patterns of the somitic marker gene *Meox1* (formerly *Mox1*; ref. 23) in individual somites of a Theiler stage[24] (TS) 18 mouse embryo (Fig. 2*a*). At the organ level, we have reconstructed the expression pattern of the myogenic marker gene *Myf5* (ref. 25) in the rostral thorax and in the forelimb anlagen of a TS18 mouse embryo (Fig. 2*b*). And at the level of the whole embryo, we have reconstructed the entire expression pat-

[1]*Integrative Morphology Group, Department of Anatomy, University of Vienna, Vienna, Austria.* [2]*Institute of Mammalian Genetics, GSF-National Research Center for Environment and Health, Neuherberg, and Department of Molecular Biology, CNRS URA 1947, Pasteur Institute, 25 rue du Dr. Roux, 75724 Paris Cedex15.* [3]*Department of Molecular and Cellular Biology, TRANSGENE S.A., Strasbourg, France. Correspondence should be addressed to J.S. (e-mail: johannes.streicher@univie.ac.at).*

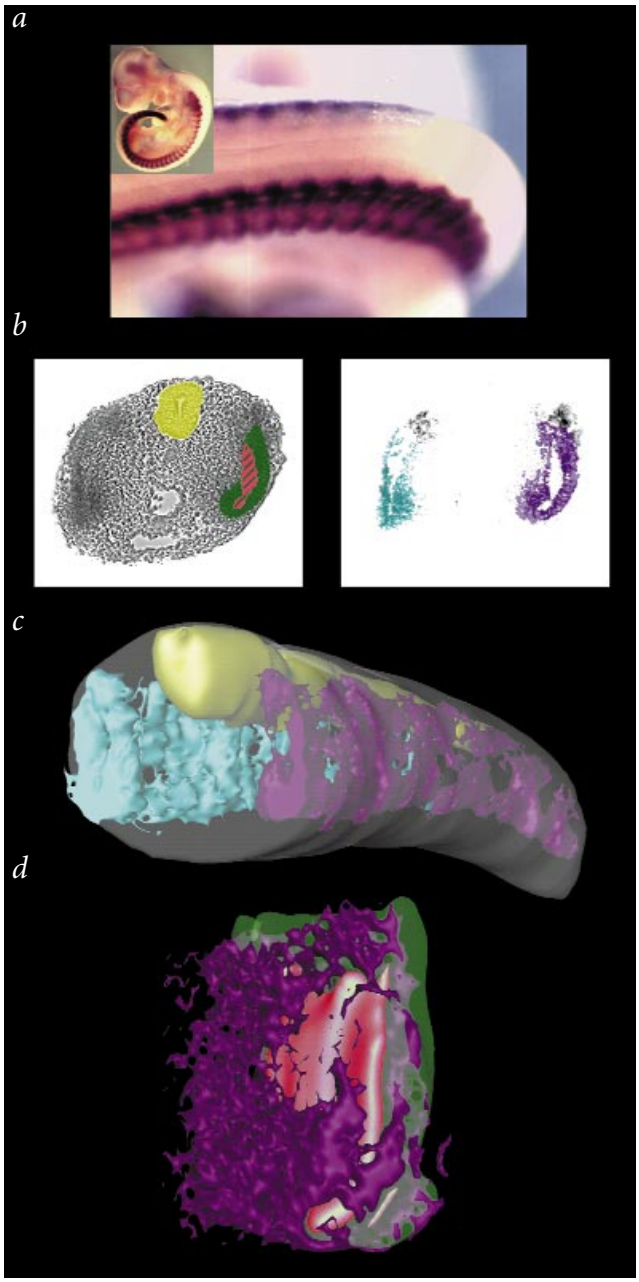

Fig. 1 Illustration of the 3D-reconstruction concept. ***a***, TS18 mouse embryo analysed by WISH for *Meox1* expression. The higher magnification shows a dorso-lateral view of the left paraxial trunk region at the level of the hindlimb bud. ***b***, Phase-contrast image (left) and bright-field image (right) of a sample cross-section at the caudal level. In the phase-contrast image, the morphological structures segmented for reconstruction are marked by coloured overlays: green, histologically differentiated somite (dermomyotome and myotome); red stripes, myotome; yellow, neural tube. In the bright-field image, the *Meox1* signal from the right (blue) and left (purple) sides are segmented separately. Signal-expressing areas outside of the overlays belong to neighbouring somites. ***c***, 3D reconstruction of a tail segment showing the tail surface (transparent grey), the *Meox1* expression signals of both sides (blue and purple) and the neural tube (yellow). ***d***, Selective 3D reconstruction of one somite. Green, histologically differentiated somite; purple, *Meox1* signal; red, central signal-free space.

tern of the neuronal marker gene *Scgn10* (formerly *Scg10*; refs 26,27) in a TS17 mouse embryo (Fig. 2c).

Gene expression in developmental subunits

The high-resolution 3D reconstruction of individual somites revealed new aspects of the *Meox1* expression pattern. WISH permits the recognition of gross differences of the expression signal within a somite, and sectional staining helps to attribute the signal to certain somite derivatives, but 3D reconstruction enables the distinction of regional differences throughout the entire somite and within its derivatives. In particular, somite derivatives that appear to express no or low levels of *Meox1* in the whole-mount (Fig. 1*a*) can be dissected into three distinct territories with the help of 3D reconstruction: the myotome, the rostro-medial moiety of the sclerotome and the lateral-most layer of the dermomyotome (Fig. 2*a*). Moreover, the reconstruction provides evidence that *Meox1* expression extends beyond the caudal boundary of the somite (Fig. 2*a*).

The relevance of a reliable and detailed mapping of expression territories to subregions of embryonic primordia is underlined by recent observations showing that subtle differences in the rostro-caudal and dorsoventral distribution of expression territories have a crucial role in vertebrate axial patterning[28,29].

Gene expression at the developing organ level

Studies of larger and more complex developing units, such as head, limb or inner organ systems, are frequently hampered by overlaps of signals from superficial and deep structures and by compromised visibility due to optical tissue interference in WISH preparations. In most cases, the detailed 3D arrangement of gene expression preceding morphological differentiation is difficult to determine. As our technique generates a comprehensive 3D representation of all signal-expressing areas, subcompartments of gene-expressing cell populations can be explored in their spatial arrangements. This provides images of molecular subdivisions of as yet undifferentiated blastemata.

The reconstruction of *Myf5* signals in a thoracic body region (Fig. 2*b*) reveals two subregions of the gene-expressing area, reflecting the bipartite morphology of the myotome in inter-limb somites[30]: a smaller dorsal portion corresponds to the epaxial myotome, and a ventrally elongated portion corresponds to the hypaxial myotome. In the limb, a detailed 3D analysis enables the distinction of different *Myf5*-positive cell populations in the undifferentiated myogenic blastemata invading the limb bud (Fig. 2*b*). We discerned two dorsal and two ventral subpopulations (Fig. 2*b*, right). In the proximal (stylopod) portion of the limb bud, the four subpopulations together form a circle around the central, prechondrogenic core (Fig. 2*b*, right). Only two *Myf5*-positive populations extend further distally into the prospective zeugopod portion of the limb, forming separate dorsal and ventral branches (Fig. 2*b*, right). These subtle aspects of gene-expression topology cannot be seen in the whole-mount and cannot easily be deduced from single sections.

Gene expression in whole-body screens

At the whole-embryo level, WISH preparations are primarily used to screen for relevant expression patterns of new genes and for interesting phenotypes in genetically modified organisms. To investigate the advantage of 3D reconstructions for these purposes, we reconstructed an entire TS17 mouse embryo hybridized for the neuronal marker gene *Scgn10* from 478 sections. Despite the lower microscopic resolution necessary for capturing complete sections through a whole embryo, it is possible to accurately visualize the topology of signal-expressing regions (Fig. 2*c*).

The immediate digital enlargement capability of the 3D models represents a major advance over conventional screening techniques. For instance, the whole-mount embryo hinted at different intensities of *Scgn10* signal expression near the anlage of the trigeminal ganglion. Therefore, after enlargement of the

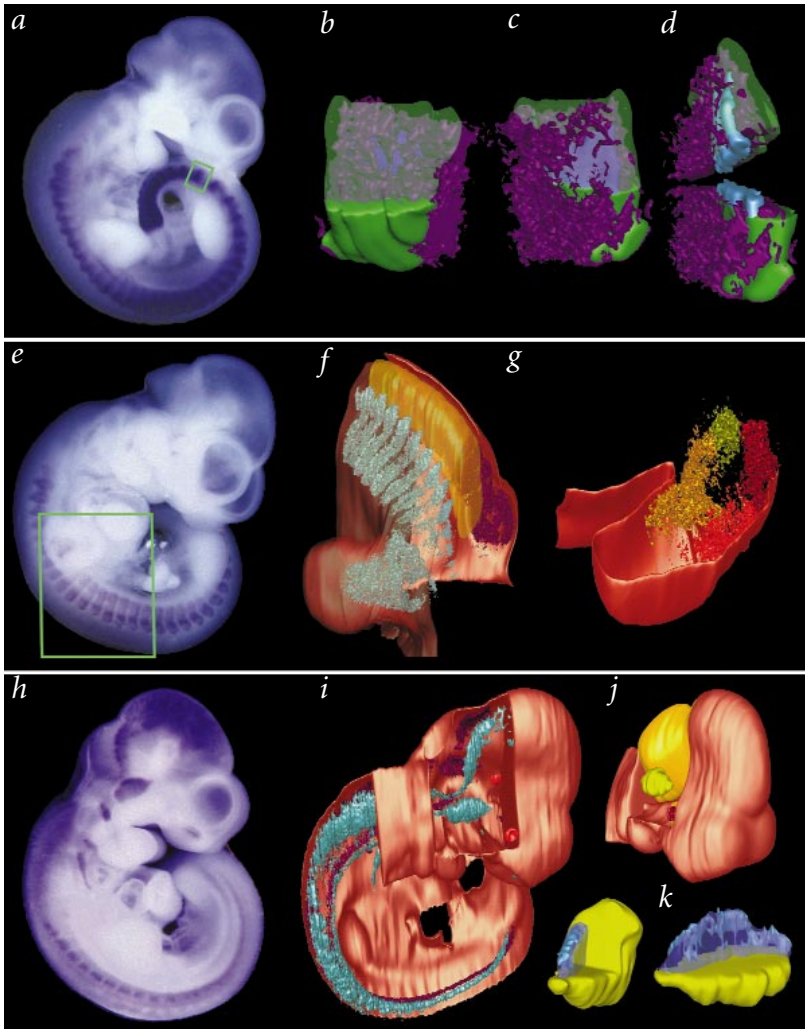

Fig. 2 3D models of embryonic structures and gene expression patterns, demonstrating reconstructions from three different structural levels. *Meox1* expression in a TS18 WISH embryo (***a***) and selective reconstruction of a sacral somite (17 sections cut at 5 μm; total size, 85 μm) are shown. The box indicates the reconstructed somite (sacral somite 1, according to ref. 41). Lateral (***b***), medial (***c***) and split (***d***) views are shown of the reconstructed somite. Green, surface of the histologically differentiated somite (dermomyotome and myotome), the dorsal half is rendered transparent; dark purple, *Meox1* signal outside the boundaries of the histologically differentiated somite; light purple, *Meox1* signal inside the somite; blue, central signal-free area corresponding to the myotome. The models reveal subtle features in the 3D topography of somitic *Meox1* expression that cannot be easily detected in single sections or whole mounts, such as the existence of signal-free areas in the centre of the dermomyotome (*) and the expression region of the medial side (#). The spatial relationships between histological somite, signal-positive areas and signal-free areas are best appreciated in the animated model shown on the accompanying web site (http://www.univie.ac.at/GeneEMAC). *Myf5* expression in a TS18 WISH-embryo (***e***) and reconstruction of the thoracic region (148 sections cut at 7 μm; total size, 1.036 mm) are also shown. The box indicates the reconstructed region, extending from cervical segment 4 to thoracal segment 8 (according to ref. 41). ***f***, 3D representation of the body surface (dark orange), the neural tube (yellow) and *Myf5* expression on right (silver) and left (purple) sides. (See the accompanying web site for an animated model.) ***g***, Magnified view of *Myf5* expression inside the forelimb bud (dorsal half of the surface removed; compare with Fig. 4). The model reveals four distinct *Myf5*-positive regions within the (histologically undifferentiated) limb mesenchyme: a dorsal-proximal portion (dark red), a dorsal-distal portion (bright red), a ventral-proximal portion (light green) and a ventral-distal portion (light orange). *Scgn10* expression in a TS17 WISH-embryo (***h***) and reconstruction of both the complete embryo (478 serial sections cut at 5 μm; total size, 2.49 mm) and of a small detail (trigeminal ganglion; 72 sections; total size 360 μm) are shown. ***i***, Reconstruction of the whole embryo with the body surface partially removed to expose the signals of the right (blue) and left (purple) sides. (See the accompanying web site for an animated model.) *Trigeminal ganglion. ***j***, Cranio-lateral view of the head. The window in the surface above the mesencephalic brain vesicle (yellow) exposes the anlage of the trigeminal ganglion (*); red, lens pit. ***k***, Distribution of the *Scgn10* signal (blue) inside the anlage of the trigeminal ganglion. Left, the anterior dorsal quadrant of the ganglion boundary (light green) is removed. Right, the dorsal half of the ganglion boundary (light green) is removed. *Scgn10* expression is differentially coloured for signal intensity: high signal intensity, solid blue; low signal intensity, transparent blue.

area, we represented the varying signal intensities inside the ganglion anlage by differential shading (Fig. 2*c*, right). This revealed distinct subregions of maximum signal intensity that are indiscernible in a conventional study. The *Scgn10* signal coincides with a cortical layer of cells in the neural-crest–derived dorsal portion and the trigeminal placode-derived ventral portion of the ganglion (Fig. 2*c*, right). In the dorsal portion of the ganglion, the differential representation of signal intensities reveals a rostro-caudal sequence of three foci of maximum intensity, which coincides with the three parts of the future trigeminal nerve. This indicates a very early molecular partitioning of the ganglion anlage.

Assessment of the method

To critically assess the objectivity of the reconstructed 3D models, we evaluated three criteria: (i) accuracy of the congruencing procedure; (ii) faithfulness of morphological detail; and (iii) authenticity of the segmented gene-expression patterns.

We assessed the accuracy of the congruencing procedure using an additional drill hole as a control object of known geometry and location (Fig. 3*a*). This control hole represents a part of the image that is treated in the same way as the specimen, and therefore its shape and position in the reconstructions provides a measure for the precision of the alignment of the sections. Any deviations from the regularity of the geometric shape of the control hole can be seen and quantified using vertical reslices through the stack of congruenced images (Fig. 3*b*). The statistical analysis of the coordinates of the drill hole centres in all sections showed a mean value identical (up to the first decimal place) with the original coordinates taken during drilling. The statistical variation equalled 0.35% of image width.

We evaluated the faithfulness of the reconstructed morphological structures by comparing characteristic features of the embryos before embedding with the identical features in the reconstruction models. The comparison showed no deviations of critical contours such as limb shape or gill arch arrangement. The perfect fit of the outer contours of the embryo indicated that all internal structures are faithfully reconstructed (Fig. 3*c*).

The authenticity of the reconstructed gene-expression patterns must be ascertained due to the automated signal-segmentation procedure. We assessed this property by comparing the segmentation results with the original hybridization signal of 15 randomly selected sections in each specimen. We superimposed the images of the hybridized sections with the respective segmented signal. This procedure showed that the automated thresholding reliably picks up all expression signals that differ from the background.

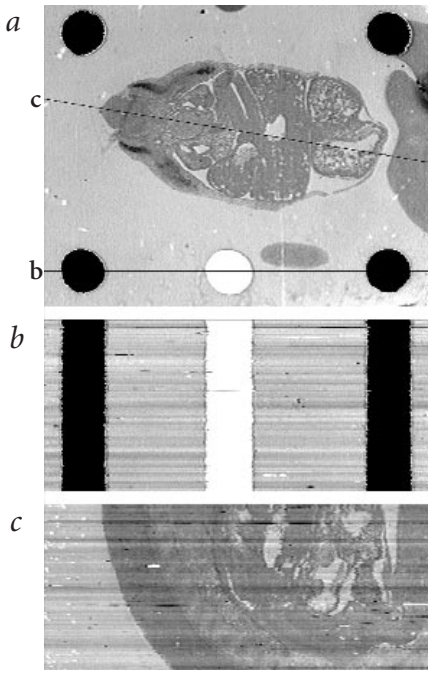

Fig. 3 Precision of the congruencing of sections. ***a***, Sample section through the thoracic region of a TS18 mouse embryo analysed by *in situ* hybridization for *Myf5* expression (dark grey). The section is counterstained with eosin. The marker holes are filled in black, and the control hole is empty. Line b, plane of reslice through the congruenced stack shown in (*b*). Line c, plane of reslice through the congruenced stack shown in (*c*). ***b***, Reslice through two marker-holes and the control hole in an automatically congruenced stack of 148 images. Note the geometric regularity of the control hole. The deviations of the individual sections can be statistically analysed. ***c***, Reslice through the specimen in the same stack as (*b*). Note the precise fit of sections along the curve of the back of the embryo (arrow) and of the internal structures.

The same is true for the discrimination of two signal intensities such as those used in the *Scgn10* expression in the trigeminal ganglion (Fig. 2*c*). The automated thresholding, however, does not relieve the operator from choosing a cutoff in a signal intensity gradient. This will always remain a subjective decision, and it is important to select the optimal threshold for each specimen. On the other hand, the chosen threshold is reliably propagated throughout the section series and provides standardization of an unavoidably subjective decision.

Versatility of the method

The 3D method presented here covers the gap of resolution and specimen size that exists between MRI microscopy[2,22] and CLSM (Table 1). The resolving power of MRI currently ends near the level of developing organs, whereas CLSM is confined to the cellular and subcellular levels. GeneEMAC can be used for the complete spectrum of resolutions required for the study of molecular markers in development, ranging from the whole-embryo level to the tissue and cellular levels. By selecting a sectional thickness between 1 and 20 µm, the z-axis resolution can be adjusted for the required level of analysis. GeneEMAC surpasses MRI microscopy in the capacity to visualize molecular signals, and CLSM in the visualization of morphological structures (Table 1). If no molecular information is required, or if only subcellular molecular signals need to be visualized, MRI and CLSM represent the techniques of choice for 3D reconstruction, because no physical sectioning and no congruencing is necessary.

The present version of GeneEMAC is adjusted for the visualization of gene-expression signals in developing morphological entities. For this purpose, grey-scale images of bright-field and phase-contrast views are most suitable. If visualization of double or triple hybridizations is required, an additional visualization mode, such as fluorescence imaging or colour imaging, can be used for a reliable separation of the signals. GeneEMAC can be adapted for these techniques, but a considerable increase in the amount of data has to be taken into account and a colour-based threshold definition must be implemented.

Publication of 3D data

Many 3D-rendering software packages (for example Velocity[2]) offer the possibilities to shift, rotate and spin a model, to zoom in and out, to switch between parts of models, and to select parts for combined viewing. This permits study and quantitative analysis of gene-expression patterns in their complete 3D topology. A faithful presentation of this information requires advanced visualization techniques.

For publication in printed media, red-cyan or colour stereopairs (Fig. 4) represent the best choice, but stereoscopic views are often unsatisfactory for revealing complex topological detail. Digital 3D models are ideally suited for electronic publication of gene-expression data, as the reader will be able to explore data generated in distant laboratories in great detail. At present the best form of visualization is movies derived from different views of a 3D model, or interactive models that can be moved at will by the viewer. QuickTime (QT, Apple Computer) and QuickTime Virtual Reality (QTVR, Apple Computer) movies represent the most widespread animation formats. These can be integrated into web pages and viewed independently of the platform used. Alternatively, Java 2 (Sun Microsystems) allows the viewing of QT and QTVR movies in a browser-independent manner. QT movies enable the viewer to observe pre-selected sequences of views, whereas QTVR makes it possible to explore the models interactively. Examples of QT- and QTVR-animated models of the reconstructions presented here are available (http://www.univie.ac.at/GeneEMAC).

Besides the advantages of publishing 3D models of gene-expression data directly on the web, such models may also have a role in structuring future developmental databases. The 3D reconstructions contributed by different research groups can be organized into a common database, which can be queried for species, genes, developmental stages, organs, tissues and cell types (Fig. 5). The entries may consist of images, stereopairs, movies and interactive models, supplemented by browsable stacks of original sections. Links to other databases, such as the

Table 1 • Methodical range of GeneEMAC

	MRI microscopy	GeneEMAC	CLSM
sectioning mode	virtual	physical	virtual
structural level			
whole embryo	+	+	–
organ	+	+	–
tissue	–	+	(+)
cellular	–	+	+
subcellular	–	–	+
staining technique			
in situ hybridization	–	+	+
immunostaining	–	+	+
whole mount	–	+	+
visibility of morphological detail	+	+	–

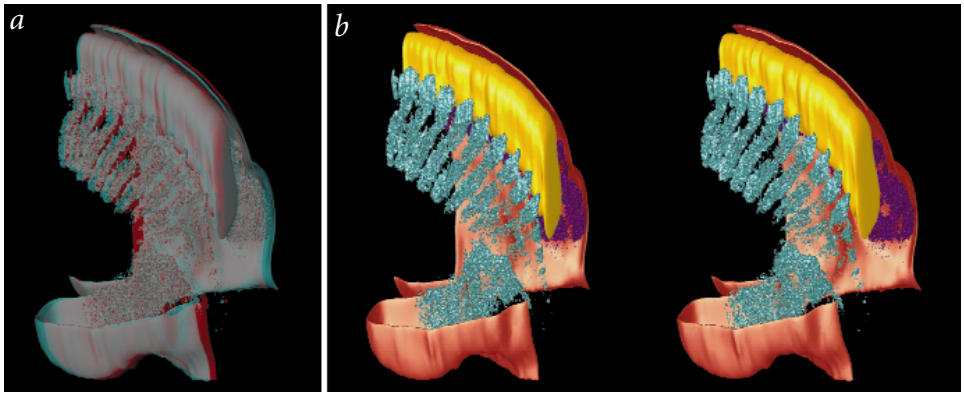

Fig. 4 Stereo-images of *Myf5* expression in the rostral thorax and forelimb anlagen of a TS18 mouse embryo (148 sections cut at 7 μm; total specimen size, 1.036 mm). ***a***, Red-cyan stereoscopic image for viewing with 3D glasses. ***b***, Stereopair for wall-eyed viewing. The body surface of the right side and the dorsal cover of the limb bud are removed. *Myf5* expression signal on the right (blue) and left (purple) sides are shown (yellow, neural tube).

mouse genome database of the Jackson Laboratory (http://www.informatics.jax.org), can provide immediate access to sequence and text-based information on the respective genes.

Discussion

3D representation techniques have begun to permeate all levels of biological analysis, from the molecular to the macroscopic scale[15,31–35]. The greatest benefit of such techniques is in areas in which complex 3D transformations take place, such as in embryonic development. By the combined representation of co-expressed genes and other molecular and cellular markers, it will be possible to create visual, 3D databases of molecular development that can be directly linked to other gene databases[1]. Eventually, by morphing 3D models of different developmental stages, 4D representations of developmental sequences and their molecular control will become possible. This will improve our understanding of the relationship between the 3D expression of developmental control genes in pattern formation and morphogenesis, and it will also help to elucidate the role of these processes in the evolution of homologous body units[36,37].

Our technique is a first step towards comprehensive, digital representation and analysis of molecular data in development. This technique already provides a number of improvements over conventional methods. First, high-resolution gene-expression data can be permanently stored as 3D models that can be interactively explored by interested researchers. Second, subtle differences in signal intensity can be visualized and permit the molecular definition of subpopulations of cells in undifferentiated tissues. Third, all information contained in the 3D models can be metrically assessed and quantified. Fourth, 3D models represent a central component of future developmental databases that will be widely accessible and directly linked to sequence and text-based databases.

Methods

Specimen preparation. We generated WISH mouse embryos with digoxigenin-rUTP labelled RNA probes for *Meox1* (ref. 23), *Myf5* (ref. 25) and *Scgn10* (ref. 27) as described[39]. The WISH embryos were embedded in glycol-methacrylate (JB4, Polysciences). Before sectioning we introduced four drill holes (300 μm in diameter) into the resin blocks in a rectangular arrangement encaging the specimen. Serial sections were cut from such blocks (5–7 μm), containing both a slice of the specimen and the permanent marker holes, which served for automated realignment and rectification processing. The sections were mounted on silane-coated slides and were cover-slipped without any additional staining.

Computer-based 3D reconstruction. We captured the section images with a videocamera (Hamamatsu C5310) mounted on a Nikon Mikrophot FXA microscope and linked to the video card of a PowerMacintosh 8600. From each section, we took two 768×512 pixel images, one phase-contrast and one brightfield, using NIH Image 1.61, a public domain image analysis software developed by NIH. Eight frames per image were averaged and corrected for uneven illumination using the built-in features of NIH Image. The images were stored in TIFF format. The phase-contrast images served for the automatic extraction of the external markers (drill holes) for the

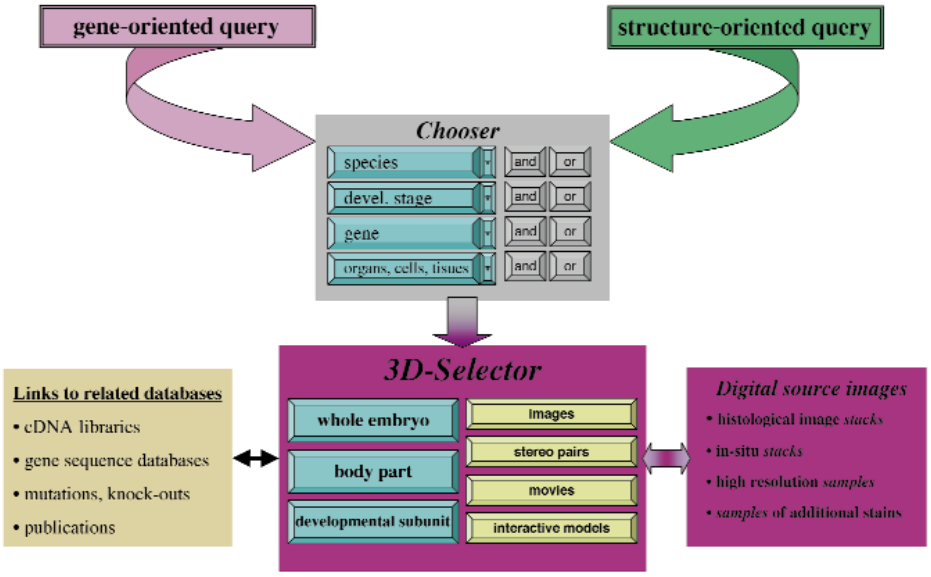

Fig. 5 Schematic organization chart for a 3D gene-expression database. The database is accessed via a 'chooser' that allows selection of the desired species, developmental stage, gene and tissue (organ, cell) in which the gene is expressed. The categories can be combined by Boolean operators. At the next level, a '3D-selector' enables a choice of resolution and type of representation of the gene-expression models. Various kinds of visualizations of the 3D models (images, stereopairs, movies, interactive models) can be selected. From every model, direct links provide access to the original sections, represented as browsable stacks of congruenced images. The models can also be directly linked to related gene databases for immediate access to the complete available information of the gene(s) represented in the model.

congruencing procedure, as well as for the segmentation of the boundaries of morphological structures. We applied no counterstains and used the bright-field images directly for segmentation of the expression signals.

We wrote special macros for the automation of all processing procedures (congruencing and segmentation) for images in a Pascal-like programming language compatible with NIH Image. We will briefly describe the macros in a language- and software-independent general format. The authentic macros are available on request.

The congruencing procedure consisted of macro-driven image-processing operations that realigned and rectified all sectional images[19]. First, the macro segmented the drill holes in each image of the phase-contrast stack and computed the locations of their centres of gravity. These coordinates were compared with the original distances measured during drilling and each image was automatically shifted, rotated and scaled to its original size and position. The parameters of these operations were recorded and subsequently applied to the corresponding bright-field image of the same section. This resulted in perfectly aligned series of images of both the phase-contrast and the brightfield stack. Subsequently, macro-driven operations segmented the desired structures from both image stacks by the use of dynamic thresholding algorithms. Individual thresholds were set once by the operator in a single sample image and were then automatically adjusted to all other images by the program. By this procedure, the macro extracted gene-expression signals and selected morphological features from the bright-field and phase-contrast images. Additional morphological features, which could not be defined by automated contour detection and filtering operations, were segmented manually. This segmentation procedure resulted in multiple series of files of binary (black and white) images, one containing the gene-expression patterns of each section and several others that each contained one of the chosen morphological structures.

We generated 3D models of the segmented structures by recombining the respective file sets into a single 3D object file using Velocity[2] (IMAGE3 LLC) running on a Unix Workstation (Octane, Silicon Graphics). The sectional outlines of a chosen structure were placed in a 3D space at a distance corresponding to the sectional thickness. Polygonal surfaces were then generated using a marching cube algorithm[39]. The final models representing the 3D reconstructions of gene-expression patterns and morphological structures can be visualized alone or as any combination of solid or transparent objects. Each model or combination of models is accessible for volumetric, stereometric and geometric analyses. For further analysis and documentation, we captured images and stereoscopic views, and recorded computer animations (movies) using the built-in functions of Velocity[2] (IMAGE3 LLC). We converted the movies to QuickTime format (QuickTime, Apple Computer) and created interactive models from movie sequences on a PowerMacintosh 8600 using QuickTimeVR (Apple Computer).

The total time expense for the reconstruction of a specimen, from the time of image capturing to the completion of the 3D-model, has an interactive (operator guided) and an automatic (macro-driven) component. Capturing a phase-contrast and a bright-field image of a section took 43 s, on average (for example, 1 h 47 min for 150 sections). Automatic congruencing of images lasted 1 m 15 s per section (about 3 h for 150 sections). Automatic segmentation took about 4 s per structure and section, whereas interactive segmentation varied considerably depending on the complexity of a structure. For a homogeneously curved outline of 300 pixels, it took about 20 s per section. File transfer and 3D-surface generation took another 20 min per model. Including the checking time after each automatic processing step, the generation of, for example, the *Myf5* expression model of the thoracic body region took 2 d, with a net workload of about 6 h for the operator.

Received 25 January; accepted 1 May 2000.

1. Ringwald, M. *et al.* A database for mouse development. *Science* **265**, 2033–2034 (1994).
2. Roush, W. A womb with a view. *Science* **278**, 1397–1399 (1997).
3. His, W. Ueber die Methoden der plastischen Rekonstruktion und über deren Bedeutung für Anatomie und Entwicklungsgeschichte. *Anat. Anz.* **II**, 382–392 (1887).
4. Born, G. Die Plattenmodelliermethode. *Archiv f. mikroskop. Anatomie* **22**, 584–599 (1883).
5. Sjöstrand, R.F. Ultrastructure of retinal rod synapses of the guinea pig eye as revealed by 3-D reconstructions from serial sections. *J. Ultrastruct. Res.* **2**, 122–170 (1958).
6. Arnolds, W.J.A. Oriented embedding of small objects in agar-paraffin, with reference marks for serial section reconstruction. *Stain Technol.* **53**, 287–288 (1978).
7. Mitchie, A. & Aggerwal, J.K. Contour registration by shape specific points for shape matching. *Comput. Graph. Image Processing* **22**, 296–308 (1983).
8. Prothero, J.S. & Prothero, J.W. Three-dimensional reconstruction from serial sections. IV. The reassembly problem. *Comput. Biomed. Res.* **19**, 361–373 (1986).
9. Huijsmans, D.P., Lamers, W.H., Los, J.A. & Strackee, J. Toward computerized morphometric facilities: a review of 58 software packages for computer-aided three-dimensional reconstruction, quantification, and picture generation from parallel serial sections. *Anat. Rec.* **216**, 449–470 (1986).
10. Braverman, M.S. & Braverman, I.M. Three-dimensional reconstruction of objects from serial sections using a microcomputer graphics system. *J. Invest. Dermatol.* **86**, 290–294 (1986).
11. Hibbard, L.S. & Hawkins, R.A. Objective image alignment for three-dimensional reconstruction of digital autoradiograms. *J. Neurosci. Meth.* **26**, 55–74 (1988).
12. Brändle, K. A new method for aligning histological serial sections for three-dimensional reconstruction. *Comput. Biomed. Res.* **22**, 52–62 (1989).
13. Moss, V.A., Jenkinson, D., McEwan, P. & Elder, H.Y. Automated image segmentation and serial section reconstruction in microscopy. *J. Microsc.* **158**, 187–196 (1990).
14. Keri, C. & Ahnelt, P.K. A low cost computer aided design (CAD) system for 3D-reconstruction from serial sections. *J. Neurosci. Methods* **37**, 241–250 (1991).
15. Rydmark, M., Jansson, T., Berthold, C.-H. & Gustavsson, T. Computer-assisted realignment of light micrograph images from consecutive section series of cat cerebral cortex. *J. Microsc.* **165**, 29–47 (1992).
16. Arraez Aybar, L.A., Merida Velasco, J.R., Rodriguez Vazquez, J. & Jimenez Collado, J. A computerised technique for morphometry and 3D reconstruction of embryological structures. *Surg. Radiol. Anat.* **16**, 419–422 (1994).
17. Verbeek, F.J., Huijsmans, D.P., Baeten, R.J., Schoutsen, N.J. & Lamers, W.H. Design and implementation of a database and program for 3D reconstruction from serial sections: a data-driven approach. *Microsc. Res. Tech.* **30**, 496–512 (1995).
18. Skoglund, T.S., Pascher, R. & Berthold, C.H. A method for 3D reconstruction of neuronal processes using semithin serial sections displayed as a cinematographic sequence. *J. Neurosci. Methods* **61**, 105–111 (1995).
19. Streicher, J., Weninger, W.J. & Müller, G.B. External marker based automatic congruencing: a new method of 3D-reconstruction from serial sections. *Anat. Rec.* **248**, 583–602 (1997).
20. Scarborough, J., Aiton, J.F., McLachlan, J.C., Smart, S.D. & Whiten, S.C. The study of early human embryos using interactive 3-dimensional computer reconstructions. *J. Anat.* **191**, 117–122 (1997).
21. Vazquez, M.D. *et al.* 3D reconstruction of the mouse's mesonephros. *Anat. Histol. Embryol.* **27**, 283–287 (1998).
22. Smith, B.R. Visualizing human embryos. *Sci. Am.* **280**, 76–81 (1999).
23. Candia, A.L. *et al. Mox-1* and *Mox-2* define a novel homeobox subfamily and are differentially expressed during early mesodermal patterning in mouse embryos. *Development* **116**, 1123–1136 (1992).
24. Theiler, K. *The House Mouse* 1–168 (Springer, Berlin, 1972).
25. Ott, M.O., Bober, E., Lyons, G., Arnold, H. & Buckingham, M. Early expression of the myogenic regulatory gene, myf-5, in precursor cells of skeletal muscle in the mouse embryo. *Development* **111**, 1097–1107 (1991).
26. Anderson, D.J. & Axel, R. Molecular probes for the development and plasticity of neural crest derivatives. *Cell* **42**, 649–662 (1985).
27. Stein, R., Mori, N., Matthews, K., Lo, L.C. & Anderson, D.J. The NGF-inducible SCG10 mRNA encodes a novel membrane-bound protein present in growth cones and abundant in developing neurons. *Neuron* **1**, 463–476 (1988).
28. Wright, D.E., White, F.A., Gerfen, R.W., Silos Santiago, I. & Snider, W.D. The guidance molecule semaphorin III is expressed in regions of spinal cord and periphery avoided by growing sensory axons. *J. Comp. Neurol.* **361**, 321–333 (1995).
29. Tajbakhsh, S. & Spörle, R. Somite development: constructing the vertebrate body. *Cell* **92**, 9–16 (1998).
30. Sporle, R., Gunther, T., Struwe, M. & Schughart, K. Severe defects in the formation of epaxial musculature in open brain (opb) mutant mouse embryos. *Development* **122**, 79–86 (1996).
31. Hosono, M. *et al.* Three-dimensional display of cardiac structures using reconstructed magnetic resonance imaging. *J. Digit. Imaging* **8**, 105–115 (1995).
32. Iwamoto, Y., Oda, Y., Tsumura, H., Doi, T. & Sugioka, Y. Three-dimensional MRI reconstructions of musculoskeletal tumors. A preliminary evaluation of 2 cases. *Acta Orthop. Scand.* **66**, 80–83 (1995).
33. Krams, R. *et al.* Evaluation of endothelial shear stress and 3D geometry as factors determining the development of atherosclerosis and remodeling in human coronary arteries in vivo. Combining 3D reconstruction from angiography and IVUS (ANGUS) with computational fluid dynamics. *Arterioscler. Thromb. Vasc. Biol.* **17**, 2061–2065 (1997).
34. Seidler, H. *et al.* A comparative study of stereolithographically modelled skulls of Petralona and Broken Hill: implications for future studies of middle Pleistocene hominid evolution. *J. Hum. Evol.* **33**, 691–703 (1997).
35. Stevens, J.K., Mills, L.R. & Trogadis, J.E. *Three-Dimensional Confocal Microscopy: Volume Investigation Of Biological Specimens* (Academic, San Diego, 1994).
36. Müller, G.B. & Wagner, G.P. Homology, *Hox* genes, and developmental integration. *Am. Zool.* **36**, 4–13 (1996).
37. Holland, L.Z., Holland, P.W. & Holland, N.D. Revealing homologies between body parts of distantly related animals by *in situ* hybridization to developmental genes: Amphioxus versus vertebrates. in *Molecular Zoology* (eds Ferraris, J.D. & Palumbi, S.R.) 267–295 (Wiley-Liss, New York, 1996).
38. Sporle, R. & Schughart, K. Paradox segmentation along inter- and intrasomitic borderlines is followed by dysmorphology of the axial skeleton in the open brain (opb) mouse mutant. *Dev. Genet.* **22**, 359–373 (1998).
39. Knox, C.K. & Wenstrom, J.C. 3D visualization of neural structures. *Proc. Eastern Multiconference Soc. Computer Simulation* 12–17 (1990).
40. Sporle, R. & Schughart, K. System to identify individual somites and their derivatives in the developing mouse embryo. *Dev. Dyn.* **210**, 216–266 (1997).